

Original Articles

Newly-developed three-band hyperspectral vegetation index for estimating leaf relative chlorophyll content of mangrove under different severities of pest and disease



Xiapeng Jiang^{a,b}, Jianing Zhen^{a,c}, Jing Miao^{a,b}, Demei Zhao^{a,b}, Zhen Shen^{a,b}, Jincheng Jiang^d, Changjun Gao^e, Guofeng Wu^{a,b}, Junjie Wang^{a,c,*}

^a MNR Key Laboratory for Geo-Environmental Monitoring of Great Bay Area & Guangdong Key Laboratory of Urban Informatics & Shenzhen Key Laboratory of Spatial Smart Sensing and Services, Shenzhen University, Shenzhen 518060, China

^b School of Architecture and Urban Planning, Shenzhen University, Shenzhen 518060, China

^c College of Life Sciences and Oceanography, Shenzhen University, 518060 Shenzhen, China

^d Guangdong Provincial Key Laboratory of Silviculture, Protection and Utilization, Guangdong Academy of Forestry, 510520 Guangzhou, China

^e Shenzhen Institutes of Advanced Technology, Chinese Academy of Sciences, Shenzhen 518055, China

ARTICLE INFO

Keywords:

Mangrove

Hyperspectral imaging

Newly-developed VIs

Pest and disease

SPAD value

ABSTRACT

Hyperspectral imaging-derived vegetation indices (VIs) have rarely been developed to estimate leaf chlorophyll content of mangrove forests under pest and disease stress. Moreover, the optimal newly-developed hyperspectral VI is generally chosen through comparison of model accuracy alone with all possible VI combinations, which might render the conclusion one-sided. With SOC710 hyperspectral images of 119 mangrove leaf samples, this study aimed to develop a new hyperspectral VI sensitive to leaf relative chlorophyll content (SPAD value) by comprehensive comparison from five aspects (estimation accuracy, sensitivity, anti-noise performance, application to simulated EnMAP and PRISMA sensors, and spatial visualization quality). Eight types of newly-developed VIs were constructed from the sensitive wavebands selected by successive projection algorithm (SPA) method, and simple linear regression model was established using each VI. The results showed that the three-band VI ($(\lambda_{757.9} - \lambda_{709.4}) / (\lambda_{709.4} - \lambda_{708.1})$) was the optimal for leaf SPAD estimation, because it had stronger correlation with SPAD, higher model accuracy of SPAD estimation using leaf and simulated hyperspectral imagers, stronger resistance to Gaussian noise, more sensitivity to extremely high chlorophyll content, and reasonable spatial visualization of SPAD. The four types of three-band VIs had higher model accuracy than the four types of two-band VIs, while two-band VIs had stronger resistance to higher Gaussian noise. Moreover, the wavelengths in the red edge region were efficient to develop hyperspectral VIs sensitive to leaf SPAD, and leaf SPAD could be more accurately estimated with pest and disease severity of 15–25%. We concluded that three-band VI consisting wavebands in the red edge region derived from leaf hyperspectral images is effective in capturing the changes of leaf chlorophyll content, which could provide great potentials for early warning of mangrove pest and disease with fine visualization details of chlorophyll content.

1. Introduction

Mangrove is one of the strongest natural ecosystems with rich ecosystem service value and productivity, which plays an important role in maintaining biodiversity and carbon sequestration (Himes-Cornell et al., 2018). The protection of mangrove is still challenging, because the structure and function of mangrove ecosystem is continuously affected

by anthropogenic factors (e.g. alien species cultivation, sea reclamation and environmental pollution) and natural factors (e.g. climate change, shoreline erosion and pest and disease infection) (Biswas et al., 2018; Luo et al., 2021; Slamet et al., 2020). In recent decades, pest and disease outbreak in mangrove forests are becoming more frequent with more diversified species of pests and larger areas of infection (Lu et al., 2019b). The damage to the cellular structure of leaves caused by pest

* Corresponding author at: MNR Key Laboratory for Geo-Environmental Monitoring of Great Bay Area & Guangdong Key Laboratory of Urban Informatics & Shenzhen Key Laboratory of Spatial Smart Sensing and Services, Shenzhen University, Shenzhen 518060, China.

E-mail address: wang_2015@szu.edu.cn (J. Wang).

and disease can lead to significant changes in chlorophyll content (Chen et al., 2018; Fourty et al., 1996), which could further threaten the health condition, net primary productivity, nutrient cycle and energy flow in mangrove ecosystem (Chen et al., 2017; Jenoh et al., 2016; Alongi, 2012). Therefore, accurate monitoring of leaf chlorophyll content is important to understand the severities of pest and disease, which could facilitate early detection of pest and disease outbreaks and improve conservation and management of mangrove ecosystem.

There are mainly two ways to obtain chlorophyll content of leaf samples collected in the field: direct laboratory chemical analysis using spectrophotometric method and indirect measurement using a portable chlorophyll meter (e.g. SPAD-502). The spectrophotometric method uses the wavelengths related to spectral absorption peaks of chlorophyll in the red region of 645–663 nm (Song et al., 2020), while the SPAD value reflects the absorption intensity in the red (650 nm) and near-infrared (940 nm) region (Chang and Chang, 2014; Morley et al., 2020). Many studies proved that the dimensionless SPAD value has strong correlation ($R^2 > 0.85$) with laboratory-based chlorophyll content (León et al., 2007), hence, the value is considered as relative chlorophyll content, and it is widely used in the field of ecological and agricultural investigation and vegetation remote sensing (Goswami et al., 2021). Moreover, chlorophyll is a major factor affecting the visible and red edge region (680–760 nm) of vegetation spectra (Curran et al., 1990; Li et al., 2017). Therefore, numerous studies use optical remote sensing data to link spectral properties with laboratory-based and relative chlorophyll content of crops (e.g. rice, corn, wheat and cotton) (Feng et al., 2020; Goswami et al., 2021; Reyes et al., 2017; Shu et al., 2021), terrestrial forest (e.g. mixed temperate forest) (Li et al., 2021) and grass (e.g. agricultural and semi-natural grassland) (Si et al., 2012). In contrast, much less attention has been paid to investigate the spectral estimation of leaf chlorophyll in coastal mangrove forest (Zhen et al., 2021; Zulfa et al., 2020).

Among the optical remote sensing data of estimating leaf chlorophyll content, hyperspectral data at the leaf (Sonobe et al., 2021; Wang et al., 2020), canopy (Hoeppner et al., 2020), airborne (e.g. AisaFenix and Pika-L sensor) (Hornero et al., 2021; Kanning et al., 2018) and spaceborne (e.g. Hyperion, CHRIS/PROBA and PRISMA) (De Grave et al., 2021; George et al., 2019; Kennedy et al., 2021; Singh and Singh, 2018) scales is more frequently employed than multispectral data (e.g. Landsat-8, Sentinel-2 and WorldView-2/3) (Flynn et al., 2020; Heenkenda et al., 2015). With hundreds or thousands of narrow spectral bands, hyperspectral data has the unique advantage of detecting subtle and detailed spectral variation in response to plant stress (Oscio et al., 2019; Sathish et al., 2021). Previous studies have proved that, hyperspectral data is more accurate in estimating leaf and canopy biochemical parameters (e.g. chlorophyll, water, and nitrogen content) than multispectral data (Baath et al., 2021; Lu et al., 2019a; Pôcas et al., 2020). In contrast to non-imaging hyperspectral data (e.g. ASD), imaging hyperspectral data could generate a large number of spectral and texture features to improve the accuracy of mapping the spatial distribution of vegetation biochemical parameters at the leaf and landscape scales (Gökkaya et al., 2015; Hoeppner et al., 2020; Lu et al., 2019a; Yu et al., 2021). Hence, many studies have employed in-situ, UAV and satellite hyperspectral images in assessing leaf chlorophyll content of crops (e.g. rice and corn), grasslands, and terrestrial forests (Jiang et al., 2021; Kanning et al., 2018; Dao et al., 2021; Tagliabue et al., 2022), however, very few studies have explored the performance of imaging hyperspectral data in quantifying leaf chlorophyll content of mangrove forest under different severities of pest and disease.

To solve the redundancy problem of hyperspectral data, many studies employ variable selection methods (e.g. successive projections algorithm (SPA) and genetic algorithm (GA)) to select informative wavelengths, and they also establish new hyperspectral vegetation indices (VIs) sensitive to leaf chlorophyll and other biochemical parameters (e.g. nitrogen and phosphorus) (Liang et al., 2018; Loozen et al., 2019). VI is a combination of two or three wavebands with simple

mathematical operations, and it is designed to enhance the sensitivity of vegetation spectral features and reduce the interference of soil and atmospheric background noises (Huete et al., 2002). In most cases, the newly-developed hyperspectral VIs sensitive to leaf biochemical parameters are chosen by exhaustive search of all possible VI combinations (Yang et al., 2021; Zhen et al., 2021). The exhaustive method is time-consuming, and several studies directly used the sensitive wavelengths chosen by a variable selection method (e.g. SPA) to construct the optimal VIs for improving computational efficiency (Dechant et al., 2017). Many studies use multivariate regression methods (e.g. partial least squares regression (PLSR), support vector regression (SVR) and random forests regression (RFR)) with sensitive wavelengths selected by variable selection methods (Dechant et al., 2017; Sun et al., 2017), and simple linear regression with the optimal VI to estimate leaf biochemical parameters (Shah et al., 2019). Moreover, some studies claimed that the VI-based simple linear regression model had a similar estimation accuracy to the multivariate regression model (Maimaitijiang et al., 2019). Generally, an optimal newly-developed VI is the best estimator of target leaf biochemical parameter through comparison of model accuracy alone (Wang et al., 2016; Yang et al., 2021), however, the conclusion might be unilateral, because little attention has been paid to the comprehensive comparison of the anti-noise performance, application to other hyperspectral sensors and mapping quality of the VI-based models.

With hyperspectral imaging data of mangrove leaves under different severities of pest and disease, this study aimed to develop a new hyperspectral VI sensitive to leaf relative chlorophyll content (SPAD value) by comprehensively comparing estimation accuracy, sensitivity, anti-noise performance, application to simulated EnMAP and PRISMA sensors, and spatial visualization quality. Eight types of newly-developed VIs were constructed from the sensitive wavebands associated with leaf SPAD, which were selected by the SPA method. This study could provide fundamental support for hyperspectral monitoring of mangrove chlorophyll content at the plot and landscape scales, and might assist for early monitoring and warning of mangrove pest and disease.

2. Materials and methods

2.1. Field sampling

The study area is located in Gaoqiao Mangrove Reserve ($20^{\circ}15' \text{--} 21^{\circ}55' \text{N}$, $109^{\circ}40' \text{--} 110^{\circ}55' \text{E}$, Fig. 1a), Zhanjiang City, Guangdong Province, China. The reserve has a southern subtropical oceanic monsoon climate with an average annual water temperature of $25\text{--}27^{\circ}\text{C}$. The area is dominated by seven mangrove species with obvious zonation characteristics, namely *Aegiceras corniculatum*, *Bruguiera gymnorhiza*, *Kandelia obovata*, *Rhizophora stylosa*, *Avicennia marina*, *Excoecaria agallocha*, and *Sonneratia apetala* (Fu et al., 2021). The leaves of pioneer species (*Aegiceras corniculatum*) are often covered by sea water at high tide, and they are easily infected by pest and disease at low tide (Ma et al., 2020). The outbreak of pest (mainly *Lasiognatha mormopa*) and disease (mainly fungal pathogen) could affect the leaf and canopy structure, leaf chlorophyll content and ecosystem function. Hence, it is important to investigate leaf chlorophyll content of *Aegiceras corniculatum* under different severities of pest and disease.

A total of 119 leaf samples (42 healthy and 77 damaged leaves) of *Aegiceras corniculatum* were collected under different severities of pest and disease (Fig. 1b and c) in December 2019, and each leaf sample had a single leaf. We randomly chose four sunlit and mature leaves from the top canopy of each tree, and a minimum distance of 10 m was kept between any two trees. For each fresh leaf, dust and salt crystal was removed from the surface; the SPAD values of left, right, top, bottom, and center (the red circle in Fig. 1c) of the leaf were measured with a SPAD chlorophyll meter (Minolta Camera Co. Ltd, Osaka, Japan), and their average value (Fig. 2, the range of SPAD value was 31.5–78.7 with

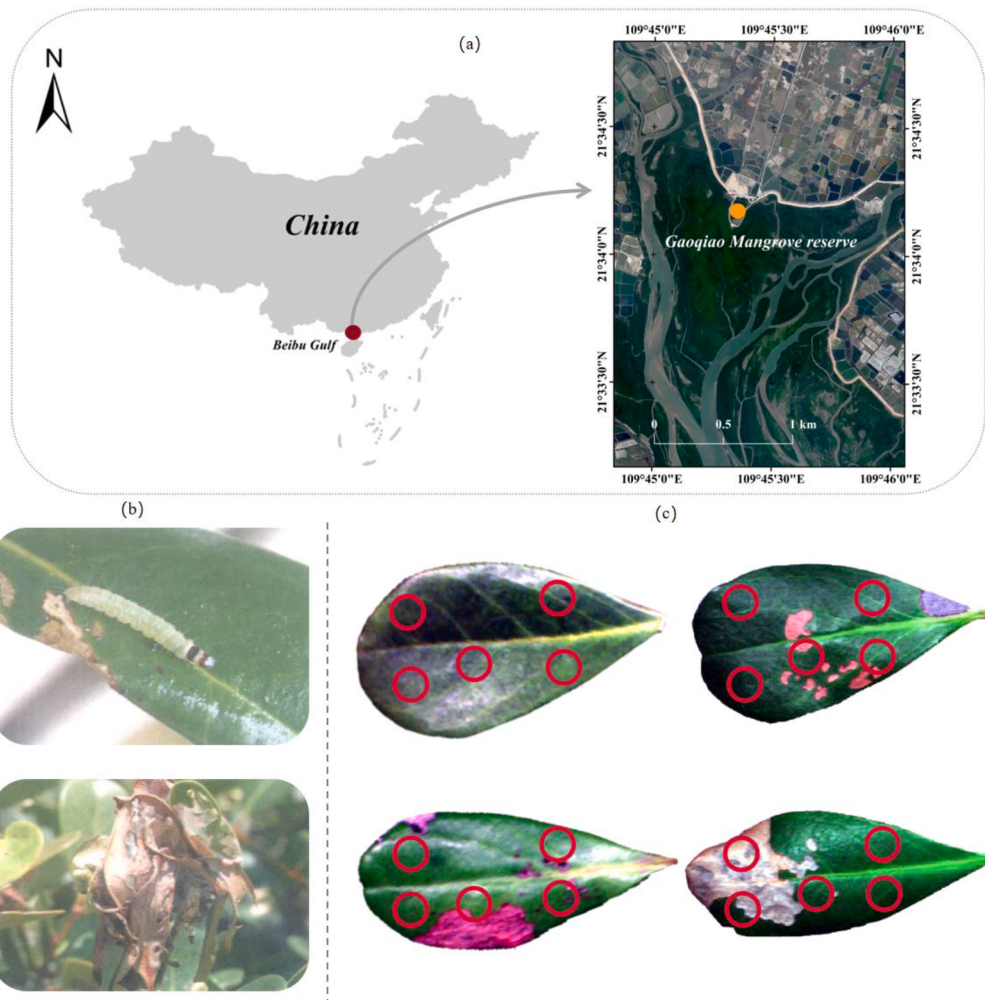


Fig. 1. Study area (a), example photographs of mangrove damaged leaves by pest and disease(b), and four true color images (Red: 640.09 nm, Green: 549.45 nm, Blue: 470.57 nm) of leaves with different severities (0, 7.1%, 18.3%, and 30.9%, from top to bottom) of pest and disease of *Aegiceras corniculatum* using SOC710 hyperspectral imaging system.

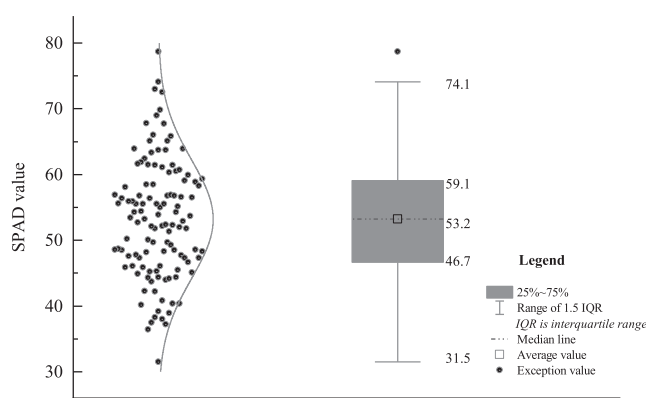


Fig. 2. Box plot of SPAD value of the 119 mangrove leaf samples.

a mean value of 53.2) was considered as relative chlorophyll content. Afterwards, each leaf was put in a labeled brown-paper envelope for hyperspectral imaging measurement.

The calculation of severity of pest and disease could refer to our previous study (Jiang et al., 2021): To accurately extract the pest and disease severity values for each leaf sample, a support vector classifier was used in ENVI 5.3 software to classify the smoothed images into three

categories (background, green healthy leaves and damaged leaves). The raster files of the healthy and damaged leaf categories were converted to vector files and further processed in ArcMap 10.5 software to edit the obvious misclassified areas. The pest and disease severity values were calculated using the formula of (pixels of damaged leaves)/(pixels of damaged leaves + pixels of healthy leaves).

The SPAD value could reflect the concentration of leaf chlorophyll *a* and *b*, which effectively indicates the potential of photosynthesis and health condition of mangrove leaves. Notably, the chlorophyll meter does not work properly with non-green and damaged leaf regions, hence, the SPAD value of each sample only reflected the relative chlorophyll content of green regions.

2.2. Leaf hyperspectral imaging data measurement and preprocessing

The hyperspectral images of leaf samples were acquired with a SOC710 portable visible and near-infrared imaging spectrometer (Surface Optics Co. Ltd, USA). Each hyperspectral image has 512 wavebands (367–1052 nm) with a spectral resolution of 1.3 nm. To reduce the effect of stray light on the quality of hyperspectral images, two 60 W halogen lamps were employed in a dark room to simulate natural light conditions. The front surface of each leaf was placed on a standard gray panel, and the vertical distance between the panel and the scanner of the spectrometer was 35 cm. The image cube of each leaf sample with the gray panel was acquired using SOC710 hyperscanner data acquisition

software. Wavelength calibration of the SOC-710 system is performed at the factory using monochromatic light sources, hence, the preinstalled calibration reflectance file and the image cube of the gray panel were used for radiometric calibration of the image cube of each leaf sample using SRAnal710 software.

To improve the ratio of signal to noise, the original 512 bands of each hyperspectral image were reduced to 450 bands (400–1000 nm) using ENVI 5.3 software, and each image was smoothed with a Savitzky-Golay smoothing filter. The mean reflectance spectra (400–1000 nm) of 119 leaf samples could be seen in Fig. S1 (Appendix 1 file).

2.3. Construction of new VIs derived from leaf hyperspectral images

To improve computational efficiency, according to the suggestion of Wang et al. (2016), our study firstly used successive projection algorithm (SPA) to select sensitive wavebands related to relative chlorophyll content (SPAD value) from the whole bands (400–1000 nm). Afterwards, the selected wavebands were employed for constructing new hyperspectral VIs. SPA is a powerful forward feature selection method (Khammohammadi et al., 2013), which uses simple projection in a vector space to search for informative variables with minimal collinearity. SPA selects a new variable that has the largest projection value on the orthogonal subspace of the previously selected variable, and all the selected variables are employed as a subset of multiple linear regression to evaluate the optimal variables with the highest validation accuracy and the lowest RMSE (Araújo et al., 2001). The selection of sensitive variables through SPA method not only effectively predicts leaf biochemical parameters, but also reduces the number of variables involved in the regression model (Guo et al., 2018).

The full dataset was randomly split into training (60% samples) and test subsets (40% samples). SPA could find sensitive bands related to SPAD value based on the lowest root mean squared error of the test subset. However, each random dataset split often lead to different combination of selected wavebands. Hence, to make the selection results more robust and reliable, 200 iterations were carried out to select sensitive wavebands with the top 20% selection frequency. The highest selection frequency could be statistically considered as the most sensitive features related to the target parameter (Jiang et al., 2021).

With the sensitive wavebands, all possible combinations of eight types of hyperspectral VIs were constructed, including four three-band VIs (VI1–VI4) and four two-band VIs (VI5–VI8). The formulas of the eight types of newly-developed VIs were mainly based on the formulas of the commonly-used VIs related to leaf chlorophyll content:

$$\text{VI1} = \frac{\lambda_a}{\lambda_b + \lambda_c} \quad (1)$$

$$\text{VI2} = \frac{\lambda_a - \lambda_b}{\lambda_a + \lambda_b - 2 * \lambda_c} \quad (2)$$

$$\text{VI3} = \frac{\lambda_b - \lambda_c}{\lambda_a} \quad (3)$$

$$\text{VI4} = \frac{\lambda_a - \lambda_b}{\lambda_b - \lambda_c} \quad (4)$$

$$\text{VI5} = \frac{\lambda_a^2 - \lambda_b^2}{\lambda_a^2 + \lambda_b^2} \quad (5)$$

$$\text{VI6} = \frac{1}{\lambda_a} - \frac{1}{\lambda_b} \quad (6)$$

$$\text{VI7} = \frac{\lambda_a - \lambda_b}{\lambda_a + \lambda_b} \quad (7)$$

$$\text{VI8} = \frac{\lambda_a}{\lambda_b} \quad (8)$$

Where λ_a , λ_b , and λ_c represents the reflectance value at the wavelength of a , b and c nm, respectively.

For each type of newly-developed VI, the Pearson's correlations of all possible VIs against SPAD value were compared, and the VI with the highest correlation was considered as the optimal newly-developed VI. Afterwards, a total of eight optimal new VIs were compared with 30 classical VIs (Appendix 1, Table S1 and S2). The classical VIs was calculated by a plug-in tool (Spectral Indices Batch, download address: <http://www.enviidl.com/appstore/>) of software ENVI 5.3.

2.4. Performance comparison of eight newly-developed VIs in SPAD estimation

To choose a suitable newly-developed VI in estimating SPAD value, we comprehensively compared the model accuracy, sensitivity, anti-noise performance, transferability to simulated hyperspectral imagries and spatial visualization in estimating SPAD value.

2.4.1. Comparing model accuracy

The full dataset was randomly split into training (60% samples) and test subsets (40% samples) 200 times, and the training subset was used for establishing simple linear regression model ($Y = k^*VI + b$), while the test subset was used for independent validation. Hence, for each of the eight optimal newly-developed VIs and optimal classical VI, a total of 200 models were constructed and validated. Each model was evaluated with determination coefficient of training and test (R^2_{Train} and R^2_{Test}) and residual prediction deviation (RPD, the ratio of standard deviation of SPAD value in the test subset to RMSE (root mean square error of validation)) (Chang et al., 2001). Using the eight VIs and optimal classical VI, their mean values of R^2_{Train} , R^2_{Test} , and RPD of the 200 VI-based linear models were calculated and compared. Moreover, each point was predicted with the composite equation based on the mean value of k and b derived from the 200 models, and the scatter points of predicted versus measured SPAD values were plotted for each type of newly-developed VIs. To explore the effect of the severity of pest and disease on the estimation accuracy of SPAD value, the whole points were split into four groups based on the severity of pest and disease: 0–5%, 5–15%, 15–25% and > 25%. Afterwards, the mean absolute relative error (MARE) was calculated for each group based on the scatter points in the estimation of SPAD value using newly-developed VIs:

$$\text{MARE} = \frac{1}{n} * \sum_{i=1}^n |(\tilde{y}_i - y_i)/y_i| \quad (9)$$

Where \tilde{y}_i is the predicted value based on the composite equation using the mean value of k and b derived from the 200 models, y_i is the measured value, n is the number of samples in each group of pest and disease severity.

2.4.2. Comparing sensitivity of newly-developed VIs to chlorophyll content with PROSPECT-5 model

To investigate whether the newly-developed VIs would saturate in the case of extremely high leaf chlorophyll content, the sensitivity to chlorophyll content was assessed for each VI using the commonly-used leaf-scale radiation transfer model (PROSPECT-5), which can simulate leaf reflectance in the region of 400–2500 nm. The PROSPECT-5 model was proposed by Feret et al. (2008) on the basis of the earliest version of PROSPECT model, which was proposed by Jacquemoud and Baret (1990). However, PROSPECT only considered equivalent water thickness (EWT) and chlorophyll content (C_{ab}) (Demarez and Gastellu-Etchegorry, 2000). The PROSPECT-5 model adopted additional four parameters (leaf structure parameter (N), leaf dry matter (C_m), leaf carotenoid content (C_{car}), and leaf brown pigment content (C_{brown})) to the model. To explore the sensitivity of VI to chlorophyll content, all the parameters except chlorophyll content were fixed (Table 1) according to the suggestion of Zhang et al. (2017) and Sun et al. (2018). The relative

Table 1

The parameters of the PROSPECT-5 model.

Parameters	Full name	Value	Unit
N	Leaf structure parameter	1.2	–
C _{ab}	Leaf chlorophyll a + b content	1–500 (step of 1)	µg/cm ²
C _{car}	Leaf carotenoid content	10	µg/cm ²
C _{brown}	Leaf brown pigment content	0	–
C _w	Leaf equivalent water thickness	0.015	µg/cm ²
C _m	Leaf dry matter	0.009	µg/cm ²

chlorophyll content (SPAD value: 31.5–78.7) was converted to the actual chlorophyll content (15.72–98.25 µg/cm²) by using the equation of $Y_{CC} = \frac{SPAD - 22.70}{0.57}$ (Connelly, 1997; Neres et al., 2020). To further calculate the sensitivity of VI to changes of chlorophyll content, the chlorophyll content in the PROSPECT-5 model was set to 1–500 µg/cm² with a step of 1 µg/cm², and the correlation between VI derived from simulated reflectance (Y axis) and chlorophyll content (X axis) was plotted for each type of VI.

2.4.3. Comparing anti-noise performance

To explore the performance of the eight newly-developed VIs against potential noises (e.g. satellite sensor, atmospheric and soil background noise), we added Gaussian noise to the original reflectance, because Gaussian noise is a normally distributed interference noise that is often used to increase spectral or image interference for spectral noise analysis (Jin and Eklundh, 2014; Tian et al., 2021). We added Gaussian noise with a variance of 0.0001, 0.0003, 0.0005, 0.0007, and 0.0009 to the original reflectance (400–1000 nm) using the Gaussian noise function in Matlab R2019b, and the higher variance indicates the stronger noise. Afterwards, the eight newly-developed VIs were recalculated using the reflectance with different levels of Gaussian noises.

To compare anti-noise performance of the eight newly-developed VIs, Pearson's correlation coefficient (r) and simple linear regression model performances (R^2_{Train} , R^2_{Test} and RPD) were compared using the reflectance with different levels of Gaussian noises. The method of constructing linear models could refer to Section 2.4.1. Moreover, the mean change rate (MCR) of r , R^2_{Train} , R^2_{Test} and RPD value using original reflectance (OR) with addition of different levels of noises was calculated for each newly-developed VI, respectively:

$$MCR = \frac{\frac{V_{GN1}-V_{OR}}{V_{OR}} + \frac{V_{GN2}-V_{GN1}}{V_{GN1}} + \frac{V_{GN3}-V_{GN2}}{V_{GN2}} + \frac{V_{GN4}-V_{GN3}}{V_{GN3}} + \frac{V_{GN5}-V_{GN4}}{V_{GN4}}}{5} \quad (10)$$

Where V is the value of r , R^2_{Train} , R^2_{Test} and RPD; GN1, GN2, GN3, GN4 and GN5 represents the original reflectance with addition of Gaussian noise with a variance of 0.0001, 0.0003, 0.0005, 0.0007, and 0.0009, respectively. MCR represents the ability to anti-Gaussian noise, indicating higher noise resistance with the MCR value closer to 0.

2.4.4. Comparing transferability to simulated hyperspectral imageries

To explore the transferability of the eight newly-developed VIs to hyperspectral satellite imageries, we simulated EnMAP (Environmental Mapping and Analysis Program) and PRISMA (PRercurso IperSpettrale della Missione Applicativa) imageries with leaf hyperspectral imaging data using spectral response function in the plug-in tool of the QGIS 3.16 software (EnMAP-Box 3, download address: <https://plugins.qgis.org/plugins/enmapboxplugin/>). EnMAP is planned for launch in 2022, it will have a medium spatial resolution of 30 m with 218 wavebands in the range of 420–2500 nm and a revisit period of 4 days (Guanter et al., 2015). The recently launched (2019, in Italy) PRISMA hyperspectral satellite (Guanter et al., 2015; Rast and Painter, 2019) has 237 wavebands with a spectral resolution of 10 nm in the range of 400–2510 nm and spatial resolution of 30 m. The eight newly-developed VIs were recalculated using the simulated EnMAP and PRISMA imageries using ENVI 5.3 software, and the wavelengths of each VI derived from the three types of hyperspectral images would be slightly different, because

they have different bandwidths and spectral resolutions. The method of constructing VI-based linear models could refer to Section 2.4.1, and the model performances (R^2_{Train} , R^2_{Test} and RPD) using the eight VIs derived from simulated EnMAP and PRISMA data were compared.

2.4.5. Comparing spatial visualization of SPAD

To investigate the spatial visualization quality of SPAD, we selected four representative leaves with pest and disease severity of 0%, 7%, 18.3%, and 30.9% for computational efficiency, and the value of each pixel in the leaf hyperspectral image was the predicted value using the composite equation based on the mean value of k and b derived from the 200 VI-based models, which were constructed in Section 2.4.1. For each leaf, the mean SPAD value of damaged and healthy regions was calculated, respectively. In theory, if the leaf with higher severity has lower SPAD value and the damaged region has lower SPAD value than the healthy region, the quality of visualization would be better.

3. Results

3.1. Correlation of newly-developed and classical VIs against leaf SPAD value

The SPA method chose a total of 22 sensitive wavelengths related to SPAD value (Fig. 3a), including nine wavebands in the red edge region (670–760 nm), five wavebands in the green region (500–560 nm), four wavebands in the blue region (400–430 nm), three wavebands in the infrared region (780–1000 nm) and one waveband in the yellow region (580–595 nm). All the wavebands had low or medium correlation with leaf SPAD value (absolute $r < 0.6$), and the reflectance at the wavelength of 545.5 nm reported the strongest correlation ($r = -0.518$, $p < 0.05$). Moreover, the reflectance in the green and red edge region was more strongly correlated with SPAD than the reflectance in the other spectral regions.

The 22 sensitive wavebands constructed 4620, 9240, 4620 and 9240 possible combinations of VI1, VI2, VI3 and VI4, respectively, while 462 combinations for the four two-band VIs. Among these combinations, the VI1 using 712.1, 998.1 and 693.3 nm, VI2 using 757.9, 713.4 and 712.8 nm, VI3 using 757.9, 708.1 and 693.3 nm, VI4 using 757.9, 709.4 and 708.1 nm, VI5 using 513.2 and 504.1 nm, VI6 using 999.5 and 713.4 nm, VI7 using 998.1 and 713.4 nm and VI8 using 998.1 and 713.4 nm reported the highest correlation with leaf SPAD ($r = -0.815$, 0.803, -0.779, 0.819, -0.660, -0.729, 0.765 and 0.772, respectively, $p < 0.05$) (Appendix 1, Fig. S2). Moreover, the three-band VIs often had higher correlations with SPAD than the two-band VIs. Each type of optimal newly-developed VI was then compared with the 30 classical VIs (Fig. 3b). Among the classical VIs, only one classical VI (REPI, red edge position index) reported $r > 0.70$ in correlating with SPAD, and the REPI showed weaker correlation than the four three-band newly-developed VIs and two two-band newly-developed VIs (VI3 and VI4).

3.2. Comparison of model accuracy with newly-developed VIs derived from leaf hyperspectral images

With the aforementioned eight optimal newly-developed VIs and REPI, a total of 200 simple linear regression models were established using each VI by randomly splitting the full dataset into training and test subsets 200 times. The results (Table 2) showed that three-band VIs (R^2_{Train} and $R^2_{Test} > 0.6$, RPD > 1.6) outperformed two-band VIs and REPI in estimating SPAD, and VI1 ($R^2_{Train} = 0.673$, $R^2_{Test} = 0.658$, RPD = 1.724) and VI4 ($R^2_{Train} = 0.671$, $R^2_{Test} = 0.671$, RPD = 1.753) reported the highest model accuracy. However, the four three-band VIs had higher CV value of RPD than the four two-band VIs and REPI, suggesting that the models using the three-band VIs had less robust estimations considering RPD value. Among the nine VIs, VI5 reported the weakest model performance in SPAD estimation, while the lowest CV value of RPD was observed for VI5. Moreover, among the four three-band VIs,

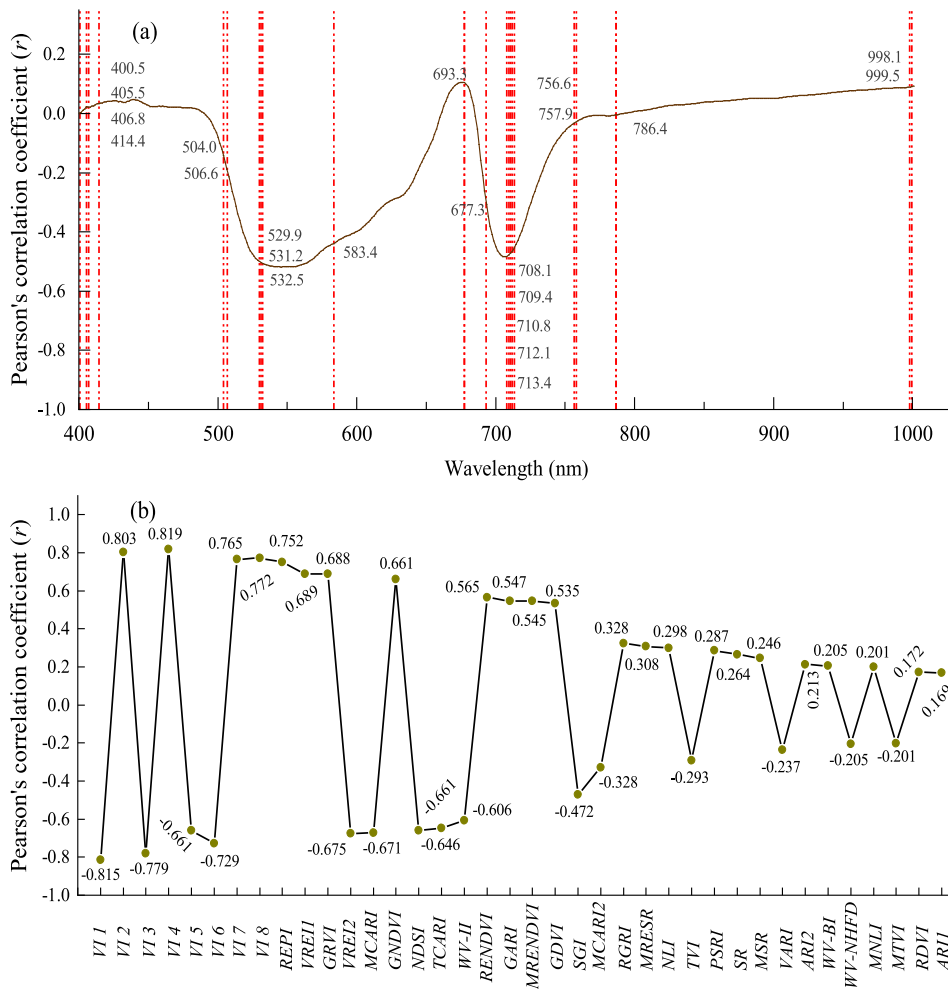


Fig. 3. Pearson's correlation coefficient of original reflectance (400–1000 nm) (a) and VIs (newly-developed and classical VIs) (b) against leaf SPAD value using all leaf samples ($n = 119$). The dotted line in the subplot (a) was the position of sensitive wavelengths selected by the SPA method. The newly-developed VIs were constructed from the selected wavelengths:

$$\text{VI1} = \frac{\lambda_{712.1}}{\lambda_{998.1} + \lambda_{693.3}}, \quad \text{VI2} = \frac{\lambda_{757.9} - \lambda_{713.4}}{\lambda_{757.9} + \lambda_{713.4} - 2\lambda_{712.8}}, \quad \text{VI3} = \frac{\lambda_{708.1} - \lambda_{693.3}}{\lambda_{757.9}}$$

$$\text{VI4} = \frac{\lambda_{757.9} - \lambda_{709.4}}{\lambda_{709.4} - \lambda_{708.1}}, \quad \text{VI5} = \frac{\lambda_{513.2}^2 - \lambda_{504.1}^2}{\lambda_{513.2}^2 + \lambda_{504.1}^2},$$

$$\text{VI6} = \frac{1}{\lambda_{999.5}} - \frac{1}{\lambda_{713.4}}, \quad \text{VI7} = \frac{\lambda_{998.1} - \lambda_{713.4}}{\lambda_{998.1} + \lambda_{713.4}} \text{ and } \text{VI8} = \frac{\lambda_{998.1}}{\lambda_{713.4}}.$$

Table 2
Performance of simple linear regression model in estimating leaf SPAD with eight newly-developed VIs and REPI.

VI	Formula	Mean value of 200 simple linear regression models			CV value of RPD	$y = k^*VI + b$	
		R^2_{Train}	R^2_{Test}	RPD		Mean k	Mean b
Newly-developed three-band VIs	$\text{VI1} = \frac{\lambda_{712.1}}{\lambda_{998.1} + \lambda_{693.3}}$	0.673	0.658	1.724	14.16%	-145.537	-136.850
	$\text{VI2} = \frac{\lambda_{757.9} - \lambda_{713.4}}{\lambda_{757.9} + \lambda_{713.4} - 2\lambda_{712.8}}$	0.646	0.647	1.679	12.86%	555.332	-435.163
	$\text{VI3} = \frac{\lambda_{708.1} - \lambda_{693.3}}{\lambda_{757.9}}$	0.614	0.607	1.611	14.98%	-185.346	106.983
	$\text{VI4} = \frac{\lambda_{757.9} - \lambda_{709.4}}{\lambda_{709.4} - \lambda_{708.1}}$	0.671	0.671	1.753	12.83%	2.888	5.123
Newly-Developed two-band VIs	$\text{VI5} = \frac{\lambda_{513.2}^2 - \lambda_{504.1}^2}{\lambda_{513.2}^2 + \lambda_{504.1}^2}$	0.443	0.432	1.317	8.63%	-60.766	17.653
	$\text{VI6} = \frac{1}{\lambda_{999.5}} - \frac{1}{\lambda_{713.4}}$	0.531	0.535	1.447	9.07%	-14.873	40.762
	$\text{VI7} = \frac{\lambda_{998.1} - \lambda_{713.4}}{\lambda_{998.1} + \lambda_{713.4}}$	0.583	0.591	1.539	8.99%	118.069	38.566
	$\text{VI8} = \frac{\lambda_{998.1}}{\lambda_{713.4}}$	0.595	0.597	1.567	9.97%	45.053	-5.029
Optimal classical VI	REPI (The wavelength position with maximum derivative reflectance at 670–760 nm)	0.568	0.567	1.511	10.61%	0.00143	962.060

* CV: coefficient of variation.

VI2 and VI 4 had lower CV value of RPD than VI1 and VI3.

Fig. 4 demonstrates the relationship of measured against predicted SPAD values of all samples derived from newly-developed VI-based models. The samples using VI4 model reported higher correlation between measured and predicted SPAD ($r = 0.82, p < 0.01$) than the other

seven VI models, and such correlations were found to be higher for the three-band VI models than the two-band VI models. Moreover, there was an obvious outlier (SPAD value = 31.5) in each subplot of Fig. 4, suggesting these VIs tend to overestimate the sample with very low leaf chlorophyll content.

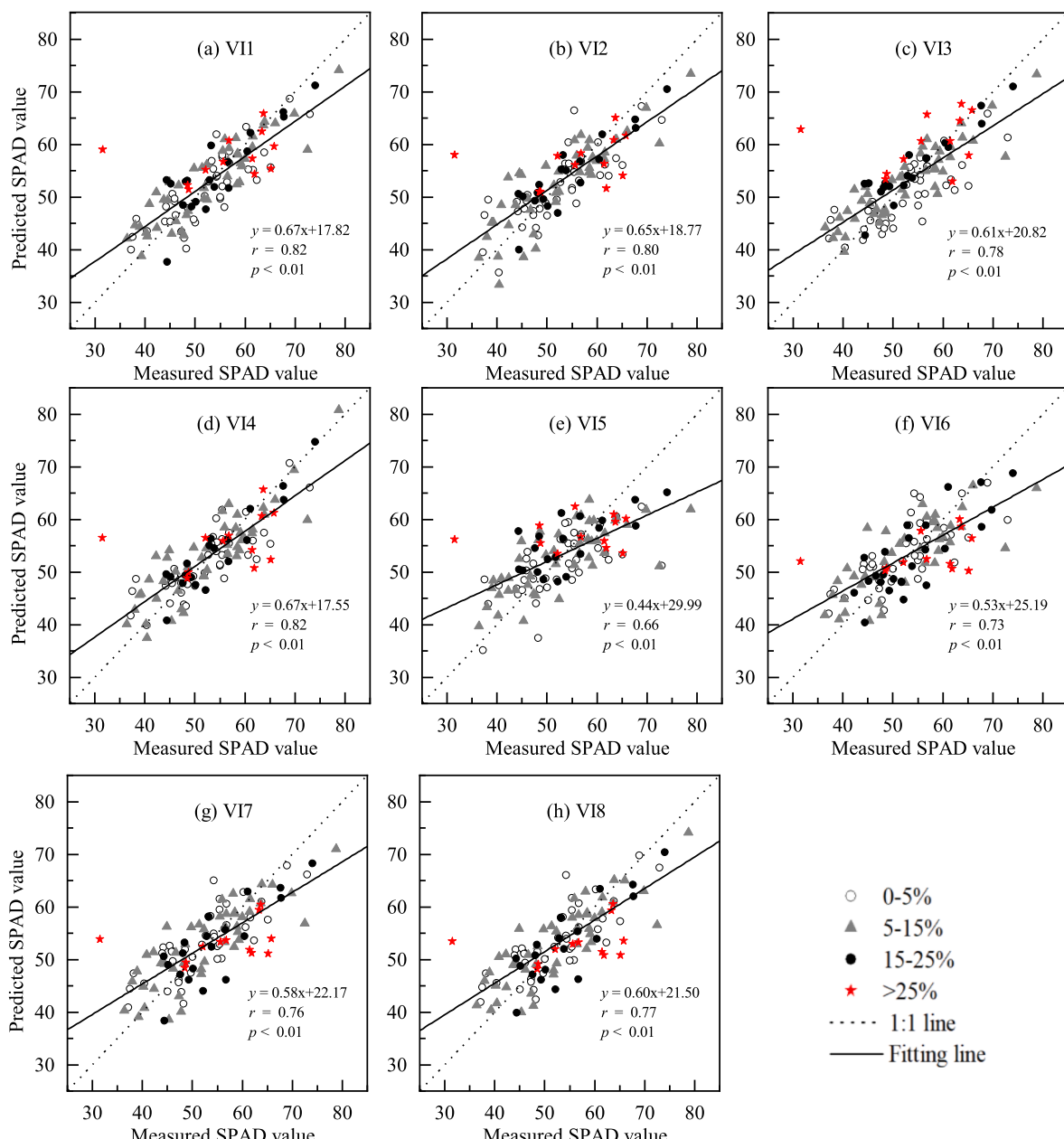


Fig. 4. Scatter plots of measured versus predicted values of leaf SPAD for each VI using all leaf samples ($n = 119$) under four levels of pest and disease severity (0–5%, 5–15%, 15–25% and > 25%). The predicted SPAD value was generated using the composite equation based on the mean value of k and b (Table 2) derived from the 200 VI-based models.

For each VI, the samples with higher pest and disease severity (>25%, MARE = 0.130–0.160) reported weaker estimations of leaf SPAD than the samples with lower severity (<25%, MARE = 0.049–0.101) (Table 3), and the samples with the severity of 15–25% had more accurate estimations of leaf SPAD than the other samples.

3.3. Comparison of sensitivity of simulated newly-developed VIs to leaf chlorophyll content using PROSPECT-5 model

Fig. 5 illustrates the sensitivity of eight newly-developed VIs simulated by PROSPECT-5 model to leaf chlorophyll content. We found that the simulated VI4, VI6 and VI8 did not tend to saturate in the case of

Table 3

The mean absolute relative error (MARE) of measured versus predicted SPAD value in estimating leaf SPAD with eight newly-developed VIs.

Severity	Number of samples	MARE							
		VI1	VI2	VI3	VI4	VI5	VI6	VI7	VI8
0–5%	42	0.074	0.074	0.077	0.071	0.089	0.087	0.083	0.082
5–15%	46	0.072	0.082	0.073	0.079	0.101	0.097	0.088	0.087
15–25%	19	0.067	0.059	0.052	0.049	0.097	0.082	0.079	0.074
> 25%	12	0.136	0.136	0.160	0.130	0.155	0.141	0.138	0.140

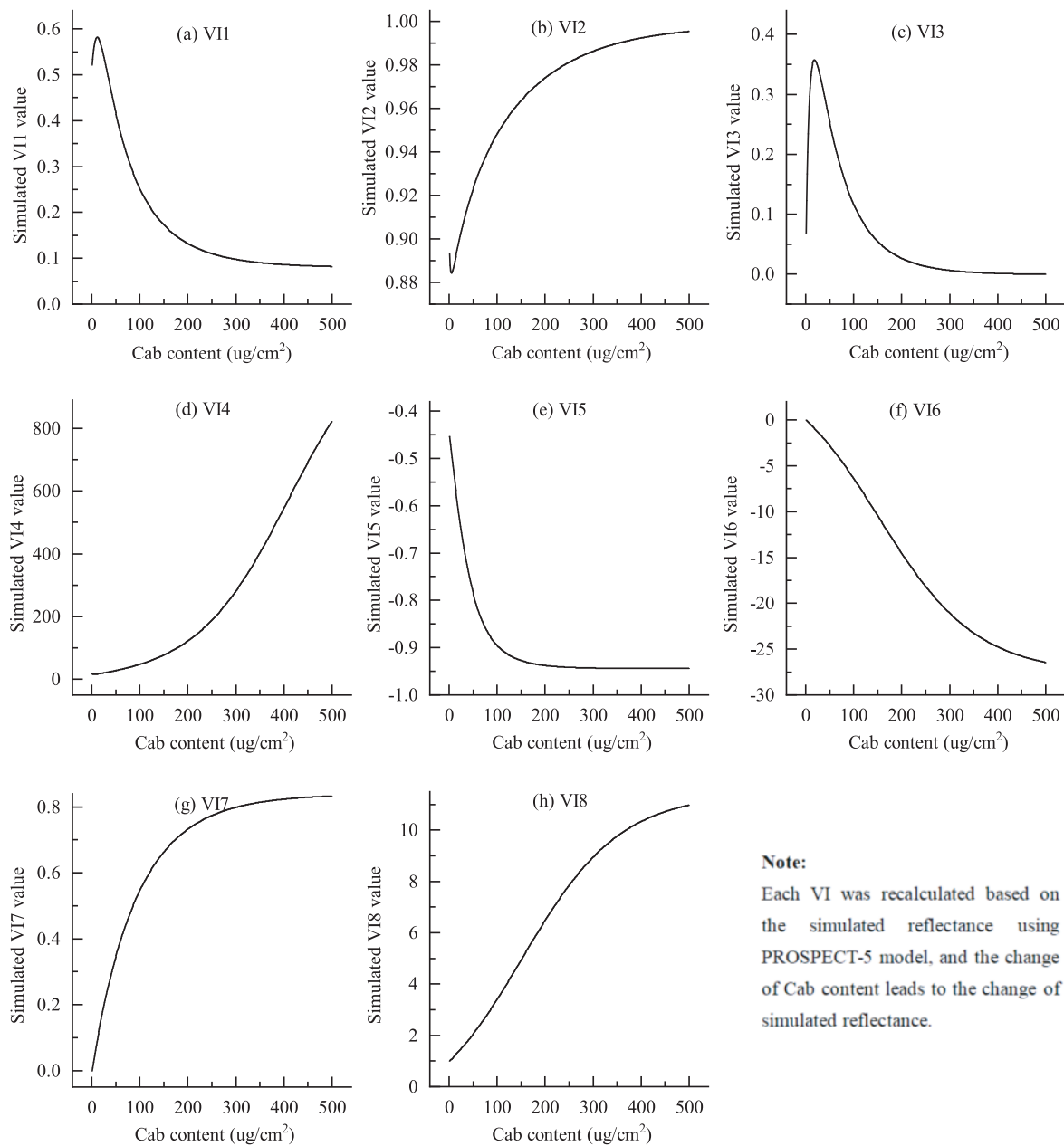


Fig. 5. The sensitivity of simulated newly-developed VIs to leaf chlorophyll content using PROSPECT-5 model.

extremely high chlorophyll content ($>450 \text{ ug/cm}^2$), while the other five VIs tended to saturate when chlorophyll content reached 200–350 ug/cm^2 .

3.4. Comparison of anti-noise performance of newly-developed VIs in leaf SPAD estimation

The VI derived from the OR with addition of stronger Gaussian noise tended to exhibit much lower correlation with leaf SPAD and much weaker model performance in estimating leaf SPAD (Table 4). For example, VII1 derived from OR reported a correlation coefficient of -0.815 with SPAD, while this value rapidly dropped to -0.393 for VII1 derived from OR with addition of Gaussian noise with a variance of 0.009. Among the four three-band VIs, VI4 showed higher noise resistance in leaf SPAD estimation, because the MCR values of r , R_{Train}^2 , R_{Test}^2 and RPD were the lowest (MCR = -0.100, -0.168, and -0.075, respectively). For VI2, the addition of relatively low Gaussian noise (GN1) made it extremely weak to estimate SPAD value (R_{Train}^2 and $R_{\text{Test}}^2 < 0.1$),

suggesting VI2 was very sensitive to Gaussian noise. Among the four two-band VIs, VI6 had higher noise resistance in leaf SPAD estimation with lower MCR values of r , R_{Train}^2 , R_{Test}^2 and RPD.

3.5. Comparison of model accuracy with newly-developed VIs derived from simulated EnMAP and PRISMA imageries

Table 5 and Table 6 demonstrates the performance of simple linear regression models with eight newly-developed VIs derived from simulated EnMAP and PRISMA imageries. Compared with the accuracy results using leaf hyperspectral images (Table 2), the eight VIs using simulated imageries reported weaker performance in leaf SAPD estimation. Among the eight VIs using simulated imageries, VI4 had the highest accuracy in estimating SPAD ($R_{\text{Train}}^2 = 0.665$, $R_{\text{Test}}^2 = 0.662$, RPD = 1.728 for simulated EnMAP; $R_{\text{Train}}^2 = 0.431$, $R_{\text{Test}}^2 = 0.443$, RPD = 1.304 for simulated PRISMA). Among the four three-band VIs using simulated EnMAP, VI2 reported the weakest performance ($R_{\text{Train}}^2 = 0.543$, $R_{\text{Test}}^2 = 0.548$, RPD = 1.427), but it had the lowest CV value of

Table 4

Performance of eight newly-developed VI models with the addition of different levels of Gaussian noise in leaf SPAD estimation.

	Gaussian noise*	VI1	VI2	VI3	VI4	VI5	VI6	VI7	VI8
Pearson's correlation coefficient (<i>r</i>)	None (OR)	-0.815	0.803	-0.779	0.819	-0.660	-0.729	0.765	0.772
	GN1	-0.709	-0.164	-0.606	0.695	-0.575	-0.656	0.687	0.695
	GN2	-0.599	-0.061	-0.498	0.633	-0.350	-0.558	0.627	0.633
	GN3	-0.470	-0.173	-0.293	0.565	-0.234	-0.507	0.570	0.565
	GN4	-0.544	-0.079	-0.212	0.510	-0.308	-0.458	0.521	0.510
	GN5	-0.393	-0.015	-0.153	0.482	-0.086	-0.525	0.506	0.482
	MCR	-0.124	-0.273	-0.100	-0.251	-0.058	-0.079	-0.090	
	R^2_{Train}	0.673	0.646	0.614	0.671	0.443	0.531	0.583	0.595
	GN1	0.510	0.033	0.373	0.463	0.334	0.435	0.472	0.481
	GN2	0.356	0.010	0.249	0.349	0.126	0.311	0.395	0.410
R^2_{Test}	GN3	0.228	0.033	0.096	0.323	0.060	0.257	0.323	0.320
	GN4	0.302	0.009	0.047	0.276	0.102	0.209	0.276	0.265
	GN5	0.158	0.002	0.029	0.259	0.020	0.281	0.259	0.235
	MCR	-0.211	-0.170	-0.447	-0.168	-0.299	-0.096	-0.149	-0.169
	None (OR)	0.658	0.647	0.607	0.671	0.432	0.535	0.591	0.597
	GN1	0.499	0.035	0.368	0.434	0.338	0.425	0.476	0.486
	GN2	0.371	0.016	0.254	0.326	0.133	0.317	0.400	0.391
	GN3	0.231	0.033	0.095	0.331	0.066	0.271	0.335	0.327
	GN4	0.302	0.019	0.056	0.213	0.105	0.226	0.277	0.268
	GN5	0.164	0.006	0.035	0.132	0.039	0.279	0.260	0.242
RPD	MCR	-0.205	-0.307	-0.423	-0.265	-0.273	-0.107	-0.150	-0.165
	None (OR)	1.724	1.679	1.611	1.753	1.317	1.447	1.539	1.567
	GN1	1.401	0.997	1.237	1.303	1.205	1.303	1.369	1.383
	GN2	1.237	0.980	1.144	1.190	1.054	1.190	1.270	1.265
	GN3	1.111	0.871	1.025	1.142	1.006	1.142	1.209	1.193
	GN4	1.165	0.957	1.008	1.119	1.031	1.119	1.153	1.138
	GN5	1.068	0.990	0.994	1.153	0.972	1.153	1.137	1.126
	MCR	-0.088	-0.080	-0.088	-0.075	-0.058	-0.043	-0.058	-0.063

* MCR: mean change rate. OR: original reflectance. GN1, GN2, GN3, GN4 and GN5 represents the OR with addition of Gaussian noise with a variance of 0.0001, 0.0003, 0.0005, 0.0007, and 0.0009, respectively.

Table 5

Performance of simple linear model in estimating leaf SPAD with newly-developed VIs derived from simulated EnMAP hyperspectral imageries. A total of 200 simple linear models were established using each VI by randomly splitting the full dataset into training and test subsets 200 times.

VI	Formula	Simulated EnMAP (mean)			CV value of RPD	$y = k \cdot VI + b$	
		R^2_{Train}	R^2_{Test}	RPD		Mean <i>k</i>	Mean <i>b</i>
Newly-developed three-band VIs	$VI1 = \frac{\lambda_{711.5}}{\lambda_{995.8} + \lambda_{690.5}}$	0.651	0.640	1.671	13.21%	-132.136	130.533
	$VI2 = \frac{\lambda_{754.5} - \lambda_{711.5}}{\lambda_{754.5} + \lambda_{711.5} - 2 \cdot \lambda_{718.0}}$	0.543	0.548	1.427	7.82%	-11.799	87.832
	$VI3 = \frac{\lambda_{704.5} - \lambda_{690.5}}{\lambda_{754.9}}$	0.602	0.595	1.582	13.50%	-169.307	96.309
	$VI4 = \frac{\lambda_{754.5} - \lambda_{704.5}}{\lambda_{704.5} - \lambda_{690.5}}$	0.665	0.662	1.728	12.69%	14.978	10.982
	$VI5 = \frac{\lambda_{532}^2 - \lambda_{502.5}^2}{\lambda_{532}^2 + \lambda_{502.5}^2}$	0.422	0.432	1.308	7.94%	-186.704	-113.877
	$VI6 = \frac{1}{\lambda_{995.5}} - \frac{1}{\lambda_{711.5}}$	0.515	0.511	1.410	7.25%	-2.658	39.663
	$VI7 = \frac{\lambda_{995.5} - \lambda_{711.5}}{\lambda_{995.5} - \lambda_{711.5}}$	0.575	0.581	1.521	9.53%	112.776	36.774
	$VI8 = \frac{\lambda_{995.5}}{\lambda_{711.5}}$	0.589	0.588	1.548	9.75%	40.882	-2.025

RPD. Among the four three-band VIs using simulated PRISMA, VI3 had the weakest performance ($R^2_{\text{Train}} = 0.031$, $R^2_{\text{Test}} = 0.073$, RPD = 0.957). Among the four two-band VIs using simulated EnMAP, VI8 was the best estimator of leaf SPAD, while VI5 had the weakest performance. In contrast, among the four two-band VIs using simulated PRISMA, VI5 was the best estimator of leaf SPAD, and VI6 had the weakest performance.

3.6. Comparison of newly-developed VIs in spatial visualization of leaf SPAD

For convenience and computational efficiency, we only investigated the spatial distribution of leaf SPAD using eight newly-developed VIs under pest and disease severity of 0% (undamaged leaf), 7%, 18.3% and 30.9% (Fig. 6). VI1, VI3, VI7 and VI8 showed that the SPAD value in damaged area was higher than that in non-damaged area, which disagreed with the fact that the damaged area was non-green area with

lower chlorophyll content. For VI5, there were no significant differences in the damaged and non-damaged areas. For VI6, at the severity of 30.9%, the non-damaged area had lower SPAD value than the damaged area. For VI2 and VI4, at the four levels of severity, the non-damaged area reported higher SPAD value than the damaged area; and the SPAD value tended to decrease with increasing severity of pest and disease.

4. Discussion

With remote sensing techniques, most studies have identified and monitored the regional extent of mangrove pests and diseases following outbreaks (Jia et al. 2019; Jiang et al., 2021; Sadeghi-Tehran et al., 2021), while few studies have quantitatively captured changes of leaf chlorophyll content during the early outbreak in mangrove ecosystem. Though several studies have developed different hyperspectral VIs to

Table 6

Performance of simple linear model in estimating leaf SPAD with newly-developed VIs derived from simulated PRISMA hyperspectral imageries. A total of 200 simple linear models were established using each VI by randomly splitting the full dataset into training and test subsets 200 times.

VI	Formula	Simulated PRISMA (mean)			CV value of RPD	$y = k^*VI + b$	
		R ² _{Train}	R ² _{Test}	RPD		Mean k	Mean b
Newly-developed three-band VIs	VI1 = $\frac{\lambda_{708.0}}{\lambda_{997.5} + \lambda_{688.5}}$	0.216	0.242	1.069	11.57%	-52.807	80.916
	VI2 = $\frac{\lambda_{759.5} - \lambda_{718.5}}{\lambda_{759.5} - \lambda_{718.5} - 2^*\lambda_{708.0}}$	0.23	0.274	1.067	13.81%	82.759	17.689
	VI3 = $\frac{\lambda_{708.0} - \lambda_{698.5}}{\lambda_{759.5}}$	0.031	0.073	0.957	12.27%	-28.56	58.59
	VI4 = $\frac{\lambda_{759.5} - \lambda_{708.0}}{\lambda_{759.5} - \lambda_{698.5}}$	0.431	0.443	1.304	12.97%	10.718	27.795
	VI5 = $\frac{\lambda_{530.0}^2 - \lambda_{507.0}^2}{\lambda_{530.0}^2 + \lambda_{507.0}^2}$	0.296	0.289	1.162	8.10%	-199.885	-129.414
	VI6 = $\frac{1}{\lambda_{997.5} - \lambda_{718.5}}$	0.037	0.082	0.924	18.93%	-0.324	52.558
	VI7 = $\frac{\lambda_{997.5} - \lambda_{718.5}}{\lambda_{997.5} + \lambda_{718.5}}$	0.075	0.129	0.963	13.40%	25.433	51.430
	VI8 = $\frac{\lambda_{997.5}}{\lambda_{718.5}}$	0.027	0.099	0.946	16.56%	3.334	49.443

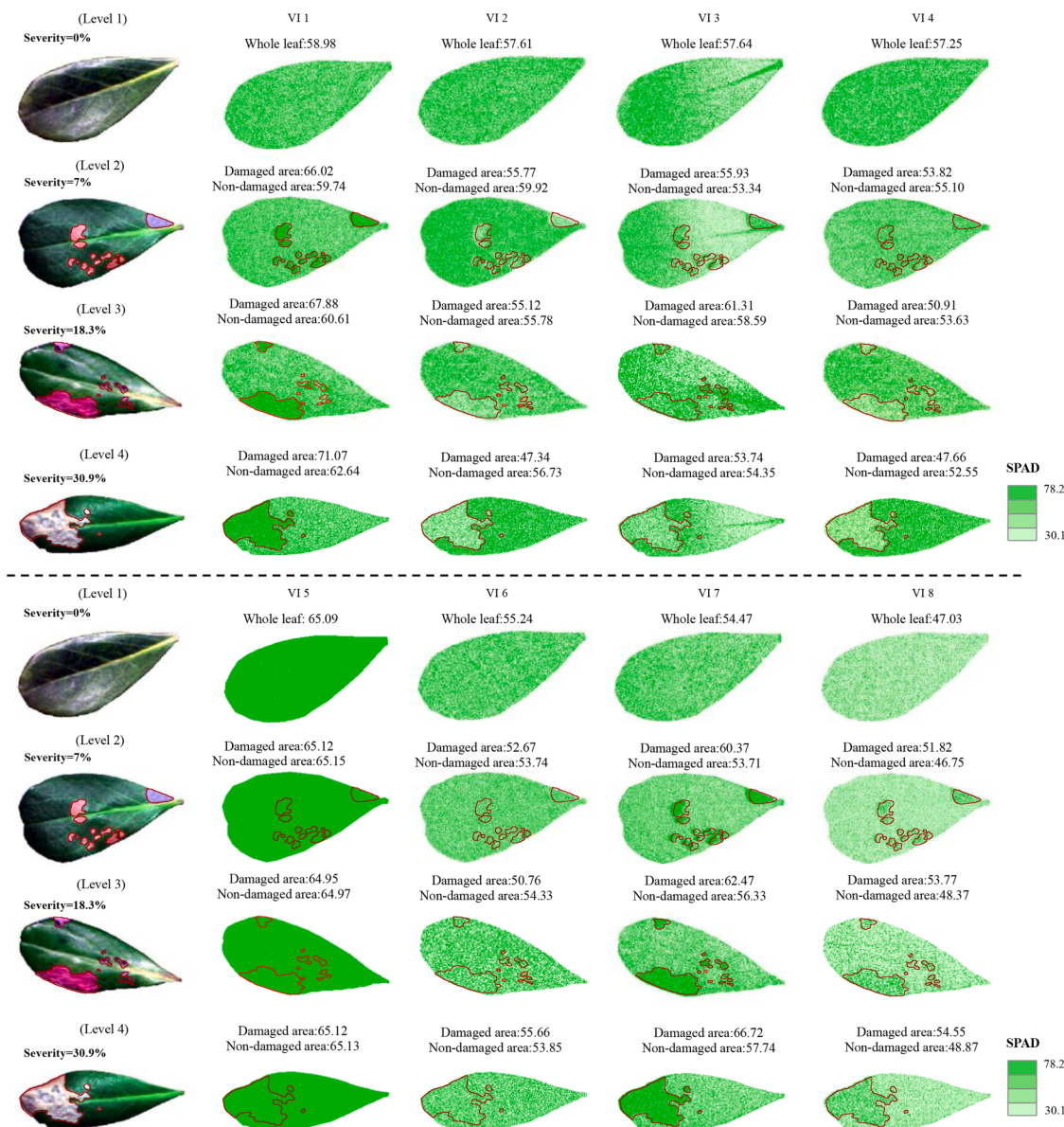


Fig. 6. Visualization of leaf SPAD value using the composite equation based on the mean value of k and b derived from the 200 simple linear regression models with each newly-developed VI.

correlate with leaf chlorophyll content (Jia et al., 2019), they often compared model accuracy alone to choose an optimal VI among numerous possible VIs. To avoid the one-side approach with some uncertainties, we comprehensively compared five aspects (model accuracy, sensitivity, anti-Gaussian noise performance, transferability to simulated hyperspectral imageries, and spatial visualization) to choose a reliable hyperspectral VI for estimating relative leaf chlorophyll content (SPAD value) from the eight types of newly-developed VIs. The results revealed that VI4 ($(\lambda_{757.9} - \lambda_{709.4}) / (\lambda_{709.4} - \lambda_{708.1})$) was a suitable estimator of leaf SAPD, because it had the stronger correlation with SPAD (Fig. 3b), higher model accuracy of SPAD estimation using leaf hyperspectral data (Table 2) and simulated hyperspectral imageries (Table 5 and Table 6), stronger resistance to Gaussian noise (Table 4), more sensitivity to extremely high chlorophyll content (Fig. 5), and reasonable spatial visualization of SPAD (Fig. 6).

The formula of VI4 ($(\lambda_a - \lambda_b) / (\lambda_b - \lambda_c)$) was developed based on the modified Datt index ($(\lambda_{719} - \lambda_{726}) / (\lambda_{719} - \lambda_{743})$) that was proposed by Lu et al. (2015), who demonstrated that this index was an optimal index for remote estimation of chlorophyll content in plants with varying leaf surface structures (Lu et al., 2015). Lu et al. (2018) further proved that this type of VI was an optimal index for the remote estimation of vegetation chlorophyll content across several plant species in different growth stages (Guo et al., 2018). Zhao et al. (2019) also demonstrated this type of VI was the most effective for estimating the chlorophyll content for both leaf surfaces of various species. The encouraging results of the modified Datt index could be explained by that all the three wavebands are in the red edge region (680–760 nm), which is very sensitive to leaf chlorophyll content (Li et al., 2017; Li et al., 2019). Similar to the eight VIs developed in our study (Table 2), many studies have developed hyperspectral VIs containing at least one waveband in the red edge region to quantify leaf chlorophyll content (Guo et al., 2019).

Four newly-developed VIs (VI1, VI6, VI7 and VI8) employed the infrared wavelength of 998.1 nm, which is related to leaf structure and water content (Zovko et al., 2019). This could be explained by that leaves damaged by pest and disease could change leaf biochemistry and structure, and could further affect leaf spectral characteristics. At present, most VIs sensitive to leaf chlorophyll content are developed for healthy green leaves or canopies of crops (Liang et al., 2016). In addition, all the eight newly-developed VIs had lower estimation error of chlorophyll content at the relatively lower severity of pest and disease (15–25%, Table 3). Therefore, the newly-developed VIs might have great potentials in early warning of mangrove pest and disease, and these VIs are still required to be validated with crops and terrestrial forest.

In remote estimation of mangrove chlorophyll content, Zhen et al. (2021) and Jia et al. (2019) developed new VIs from Sentinel-2 images, Heenkenda et al. (2015) used random forest regression to associate WorldView-2 satellite image bands and their spectral transformations with canopy chlorophyll, and Zhao et al. (2019) developed new VIs from ASD leaf hyperspectral data. To our knowledge, this study was the first to utilize eight types of newly-developed hyperspectral VIs derived from leaf hyperspectral images in quantifying mangrove leaf relative chlorophyll content under different pest and disease severities. All the newly three-band VIs reported RPD values of 1.6–1.8 (Table 2), suggesting the VI-based simple linear regression models are average models with medium accuracy (Chang et al., 2001). Moreover, the leaf hyperspectral images could finely reflect the spatial distribution of leaf SPAD (VI2 and VI 4 in Fig. 6), which is helpful for precision management of plant stress and health. However, the poor visualization of leaf SPAD for some newly-developed VIs (VI1, VI3, VI5, VI7 and VI8 in Fig. 6) might mislead the identification and distribution of pest and disease, hence, it is of great importance to choose VIs with reliable visualization of leaf SPAD.

The majority of classical VIs reported much weaker correlation with leaf SPAD than the newly-developed VIs (Fig. 3b), Zhao et al. (2019) and Zhen et al. (2021) demonstrated similar results in performance

comparison of newly-developed and previous VIs for leaf chlorophyll estimation, this might because the performance of VI is strongly affected by plant species, regions, seasons or remote sensing sensors. Moreover, the three-band newly-developed VIs outperformed two-band VIs considering model accuracy (Table 2), which agrees with the results of Zhen et al. (2021) and Yang et al. (2021), because three-band VIs have more spectral information, and they are more sensitive to chlorophyll content than two-band VIs (Fig. 5). However, under the condition of adding higher level Gaussian noise to original reflectance, three-band VIs had weaker model performance than two-band VIs (Table 4), suggesting that three-band VIs could only be resistant to low noises. Hence, it is important to enhance signal-to-noise ratio (e.g. smoothing and spectral transformation methods) before VI construction. On the other side, all the new VIs were developed from sensitive wavebands that were selected by multiple iterations of SPA method, because the majority of wavebands are redundant. This VI construction method is time-saving and effective (Wang et al., 2016), because the new VIs were constructed from just 22 wavebands and greatly decreased the combinations of all possible construction. However, it is uncertain whether the selected wavebands cover all the important bands related to leaf SPAD by using a single variable selection method. Therefore, future work should focus on the integration of different variable selection methods (e.g. genetic algorithm, recursive feature elimination, and eXtreme Gradient Boosting) to establish a union set of important wavebands sensitive to leaf SPAD for new VI construction.

There are much fewer hyperspectral satellites in orbit (e.g. PRISMA in Italy and Zhuhai-1 in China) than multispectral satellites (e.g. Sentinel-2 and WorldView-2/3). Hence, very little attention has been paid to quantify leaf chlorophyll content of mangrove with space-borne hyperspectral data. We simulated PRISMA and upcoming EnMAP hyperspectral data based on leaf hyperspectral images (Table 5 and Table 6), and found that the newly-developed VIs using simulated EnMAP data (RPD = 1.308–1.728) outperformed those using simulated PRISMA (RPD = 0.924–1.304), suggesting that the newly-developed VIs have great potentials to be transferred to EnMAP sensor in estimating mangrove leaf chlorophyll content, which might facilitate health management of mangrove forests at the landscape or region scale. Several studies have employed simulated EnMAP hyperspectral imagery for forest aboveground biomass mapping (Cooper et al., 2021), fractional shrub cover estimation (Schwieder et al., 2014), and retrieval of seasonal leaf area index (Locherer et al., 2015). To our knowledge, this study was the first to investigate the performance of simulated EnMAP imagery in mangrove leaf chlorophyll estimation. However, there are still some key problems to be considered for upscaling of SOC leaf hyperspectral images to simulated hyperspectral imageries, including unmatched spatial resolution, differences of coordinate system and differences between leaf and canopy reflectance.

PROSPECT model is an efficient tool to investigate the performance of newly-developed and traditional hyperspectral VIs (Qiao et al., 2020). Gupta and Pandey (2021) and Yue et al. (2021) utilized PROSPECT-based VIs in estimating leaf chlorophyll content and leaf area index. We only employed PROSPECT-5 model and varying chlorophyll content to explore the sensitivity of newly-developed VIs to leaf chlorophyll content, but the remaining parameters of PROSPECT-5 with fixed values might also have an impact on the sensitivity of the new VIs. Therefore, subsequent studies will combine PROSPECT-5, the other parameters with varying values and statistical models to estimate mangrove leaf chlorophyll content. Moreover, there were only limited leaf samples for each group of severity of pest and disease, and we did not develop new VIs applied to different groups. Hence, it is required to investigate VIs sensitive to different levels of pest and disease using UAV or satellite hyperspectral images, which could facilitate understanding the spectral mechanism of pest and disease at the landscape scale, and providing early warning of pest and disease for sustainable protection in mangrove ecosystem.

5. Conclusion

Based on sensitive wavebands selected by the SPA method, we constructed eight types of newly-developed hyperspectral VIs, and further comprehensively compared their performance in estimating mangrove leaf relative chlorophyll content (SPAD value) under different severities of pest and disease from five aspects, the main conclusions could be drawn as follows:

The three-band VI ($(\lambda_{757.9} - \lambda_{709.4}) / (\lambda_{709.4} - \lambda_{708.1})$) was the optimal VI for leaf SPAD estimation considering model accuracy using leaf hyperspectral images, sensitivity to leaf chlorophyll content, anti-noise performance, transferability to simulated EnMAP and PRISMA and spatial visualization quality;

Three-band VIs had higher model accuracy in leaf SPAD estimation than two-band VIs, while two-band VIs had stronger resistance to higher Gaussian noise;

The wavelengths in the red edge region were effective to develop two-band or three-band hyperspectral VIs sensitive to leaf SPAD; For each newly-developed VI, leaf SPAD could be more accurately estimated with pest and disease severity of 15–25%, which could provide great potentials for early warning of mangrove pest and disease with fine details of chlorophyll content mapping for each leaf.

The VI-based estimation of leaf chlorophyll content under pest and disease stress using hyperspectral imaging spectroscopy at the leaf scale could provide important references for early monitoring of vegetation stress and health condition in mangrove ecosystem at the landscape scale. Future work will focus on the application of the proposed three-band VI to UAV and satellite (e.g. EnMAP, PRISMA and Zhuhai-1) hyperspectral images in identifying the extent of damaged leaves infected by pest and disease and in mapping the chlorophyll content under different severities of pest and disease, which is essential for precision management of mangrove ecosystem.

CRediT authorship contribution statement

Xiapeng Jiang: Investigation. **Jianing Zhen:** Investigation. **Jing Miao:** Investigation. **Demei Zhao:** Investigation. **Zhen Shen:** Formal analysis, Visualization. **Jincheng Jiang:** Formal analysis, Visualization. **Changjun Gao:** Investigation. **Guofeng Wu:** Investigation. **Junjie Wang:** Conceptualization, Funding acquisition.

Declaration of Competing Interest

The authors declare that they have no known competing financial interests or personal relationships that could have appeared to influence the work reported in this paper.

Acknowledgements

This work was supported by Guangdong Basic and Applied Basic Research Foundation (2019A1515010741 and 2019A1515011501), Guangdong Regional Joint Fund-Youth Fund (2019A1515110400), Shenzhen Foundation for Sustainable Development (KCFZ20201221173613035), and Shenzhen Science and Technology Program (JCYJ20210324093210029).

Appendix A. Supplementary data

Supplementary data to this article can be found online at <https://doi.org/10.1016/j.ecolind.2022.108978>.

References

- Alongi, D.M., 2012. Carbon sequestration in mangrove forests. *Carbon. Manag.* 3 (3), 313–322. <https://doi.org/10.4155/cmt.12.20>.
- Aratijo, M.C.U., Saldanha, T.C.B., Galvao, R.K.H., Yoneyama, T., Chame, H.C., Visani, V., 2001. The successive projections algorithm for variable selection in spectroscopic multicomponent analysis. *Chemometr. Intell. Lab.* 57 (2), 65–73. [https://doi.org/10.1016/S0169-7439\(01\)00119-8](https://doi.org/10.1016/S0169-7439(01)00119-8).
- Baath, G.S., Flynn, K.C., Gowda, P.H., Kakani, V.G., Northup, B.K., 2021. Detecting Biophysical Characteristics and Nitrogen Status of Finger Millet at Hyperspectral and Multispectral Resolutions. *Front. Agron.* 2, 604598 <https://doi.org/10.3389/fagro>.
- Biswas, S.R., Biswas, P.L., Limon, S.H., Yan, E.-R., Xu, M.-S., Khan, M.S.I., 2018. Plant invasion in mangrove forests worldwide. *Forest Ecol. Manag.* 429, 480–492. <https://doi.org/10.1016/j.foreco.2018.07.046>.
- Chang, C.-L., Chang, K.-P., 2014. The growth response of leaf lettuce at different stages to multiple wavelength-band light-emitting diode lighting. *Sci. Horticulturae* 179, 78–84. <https://doi.org/10.1016/j.scienta.2014.09.013>.
- Chang, C.-W., Laird, D.A., Mausbach, M.J., Hurlburgh, C.R., 2001. Near-infrared reflectance spectroscopy-principal components regression analyses of soil properties. *Soil Sci. Soc. Am. J.* 65 (2), 480–490. <https://doi.org/10.2136/sssaj2001.652480x>.
- Chen, J., Shen, Z.-J., Lu, W.-Z., Liu, X., Wu, F.-H., Gao, G.-F., Liu, Y.-L., Wu, C.-S., Yan, C.-L., Fan, H.-Q., 2017. Leaf miner-induced morphological, physiological and molecular changes in mangrove plant *Avicennia marina* (Forsk.) Vierh. *Tree physiology* 37 (1), 82–97. <https://doi.org/10.1093/treephys/tpw097>.
- Chen, T., Zeng, R., Guo, W., Hou, X., Lan, Y., Zhang, L., 2018. Detection of stress in cotton (*Gossypium hirsutum* L.) caused by aphids using leaf level hyperspectral measurements. *Sensors* 18 (9), 2798. <https://doi.org/10.3390/s18092798>.
- Connolly, X.M., 1997. The use of a chlorophyll meter (SPAD-502) for field determinations of red mangrove (*Uzizophora mangle* L.) leaf chlrophyll amount. *NASA Univ. Res. Cent. Tech. Adv. Educ. Aeronaut. Space Auton. Earth Environ* 1, 187–190.
- Cooper, S., Okujeni, A., Pflugmacher, D., van der Linden, S., Hostert, P., 2021. Combining simulated hyperspectral EnMAP and Landsat time series for forest aboveground biomass mapping. *Int. J. Appl. Earth Obs.* 98, 102307. <https://doi.org/10.1016/j.jag.2021.102307>.
- Curran, P.J., Dungan, J.L., Gholz, H.L., 1990. Exploring the relationship between reflectance red edge and chlorophyll content in slash pine. *Tree physiology* 7 (1-2-3-4), 33–48. <https://doi.org/10.1093/treephys/7.1-2-3-4.33>.
- Dao, P.D., He, Y., Proctor, C., 2021. Plant drought impact detection using ultra-high spatial resolution hyperspectral images and machine learning. *Int. J. Appl. Earth Obs.* 102, 102364. <https://doi.org/10.1016/j.jag.2021.102364>.
- De Grave, C., Pipia, L., Siegmann, B., Morcillo-Pallarés, P., Rivera-Caicedo, J.P., Moreno, J., Verrelst, J., 2021. Retrieving and validating leaf and canopy chlorophyll content at moderate resolution: a multiscale analysis with the sentinel-3 OLCI sensor. *Remote Sens.* 13 (8), 1419. <https://doi.org/10.3390/rs13081419>.
- Dechant, B., Cuntz, M., Vohland, M., Schulz, E., Doktor, D., 2017. Estimation of photosynthesis traits from leaf reflectance spectra: Correlation to nitrogen content as the dominant mechanism. *Remote Sens. Environ.* 196, 279–292. <https://doi.org/10.1016/j.rse.2017.05.019>.
- Demarez, V., Gastello-Etchegorry, J., 2000. A modeling approach for studying forest chlorophyll content. *Remote Sens. Environ.* 71 (2), 226–238. [https://doi.org/10.1016/S0034-4257\(99\)00089-9](https://doi.org/10.1016/S0034-4257(99)00089-9).
- Feng, A., Zhou, J., Vories, E.D., Sudduth, K.A., Zhang, M., 2020. Yield estimation in cotton using UAV-based multi-sensor imagery. *Biosyst. Eng.* 193, 101–114. <https://doi.org/10.1016/j.biosystemseng.2020.02.014>.
- Feret, J.-B., François, C., Asner, G.P., Gitelson, A.A., Martin, R.E., Bidel, L.P., Ustin, S.L., Le Maire, G., Jacquemoud, S., 2008. PROSPECT-4 and 5: Advances in the leaf optical properties model separating photosynthetic pigments. *Remote Sens. Environ.* 112 (6), 3030–3043. <https://doi.org/10.1016/j.rse.2008.02.012>.
- Flynn, K.C., Frazier, A.E., Admas, S., 2020. Performance of chlorophyll prediction indices for *Eragrostis tef* at Sentinel-2 MSI and Landsat-8 OLI spectral resolutions. *Precis. Agric.* 21 (5), 1057–1071. <https://doi.org/10.1007/s11119-020-09708-4>.
- Fourty, T., Baret, F., Jacquemoud, S., Schmuck, G., Verdebout, J., 1996. Leaf optical properties with explicit description of its biochemical composition: direct and inverse problems. *Remote Sens. Environ.* 56 (2), 104–117. [https://doi.org/10.1016/0034-4257\(95\)00234-0](https://doi.org/10.1016/0034-4257(95)00234-0).
- Fu, S., Rao, Y., Chen, X., Zhou, X., Wu, C., Li, X., Peng, W., Cai, L., 2021. Comparison of benthic nematode assemblages in native mangrove forest and exotic mangrove plantations (*Sonneratia apetala* Buch-Ham) along the South China Coast. *Mar. Pollut. Bull.* 166, 112249 <https://doi.org/10.1016/j.marpolbul.2021.112249>.
- George, R., Padalia, H., Sinha, S., Kumar, A.S., 2019. Evaluating sensitivity of hyperspectral indices for estimating mangrove chlorophyll in Middle Andaman Island, India. *Environ. Monit. Assess.* 191 (3), 1–14. <https://doi.org/10.1007/s10661-019-7679-6>.
- Gökkaya, K., Thomas, V., Noland, T.L., McCaughey, H., Morrison, I., Treitz, P., 2015. Prediction of macronutrients at the canopy level using spaceborne imaging spectroscopy and LiDAR data in a mixedwood boreal forest. *Remote Sens.* 7 (7), 9045–9069. <https://doi.org/10.3390/rs70709045>.
- Goswami, S., Choudhary, S.S., Chatterjee, C., Mailapalli, D.R., Mishra, A., Raghuwanshi, N.S., 2021. Estimation of nitrogen status and yield of rice crop using unmanned aerial vehicle equipped with multispectral camera. *J. Appl. Remote Sens.* 15 (04), 042407 <https://doi.org/10.1117/1.JRS.15.042407>.
- Guanter, L., Kaufmann, H., Segl, K., Foerster, S., Rogass, C., Chabrilat, S., Kuester, T., Hollstein, A., Rossner, G., Chlebek, C., Straif, C., Fischer, S., Schrader, S., Storch, T., Heiden, U., Mueller, A., Bachmann, M., Mühlé, H., Müller, R., Habermeyer, M.,

- Ohndorf, A., Hill, J., Buddenbaum, H., Hostert, P., van der Linden, S., Leitão, P., Rabe, A., Doerffer, R., Krasemann, H., Xi, H., Mauser, W., Hank, T., Locherer, M., Rast, M., Staenz, K., Sang, B., 2015. The EnMAP spaceborne imaging spectroscopy mission for earth observation. *Remote Sens.* 7 (7), 8830–8857. <https://doi.org/10.3390/rs70708830>.
- Guo, P.-T., Shi, Z., Li, M.-F., Luo, W., Cha, Z.-Z., 2018. A robust method to estimate foliar phosphorus of rubber trees with hyperspectral reflectance. *Ind. Crop. Prod.* 126, 1–12. <https://doi.org/10.1016/j.indcrop.2018.09.055>.
- Guo, T., Tan, C., Li, Q., Cui, G., Li, H., 2019. Estimating leaf chlorophyll content in tobacco based on various canopy hyperspectral parameters. *J. Amb. Intel. Hum. Comp.* 10 (8), 3239–3247. <https://doi.org/10.1007/s12652-018-1043-5>.
- Gupta, S.K., Pandey, A.C., 2021. PROSAIL and empirical model to evaluate spatio-temporal heterogeneity of canopy chlorophyll content in subtropical forest. *Model. Earth Syst. Env.* 1–15 <https://doi.org/10.1007/s40808-021-01214-4>.
- Heenkenda, M.K., Joyce, K.E., Maier, S.W., de Bruin, S., 2015. Quantifying mangrove chlorophyll from high spatial resolution imagery. *ISPRS J. Photogram. Remote Sens.* 108, 234–244. <https://doi.org/10.1016/j.isprsjprs.2015.08.003>.
- Himes-Cornell, A., Pendleton, L., Atiyah, P., 2018. Valuing ecosystem services from blue forests: A systematic review of the valuation of salt marshes, sea grass beds and mangrove forests. *Ecosyst. Serv.* 30, 36–48. <https://doi.org/10.1016/j.ecoser.2018.01.006>.
- Hoeppner, J.M., Skidmore, A.K., Darvishzadeh, R., Heurich, M., Chang, H.-C., Gara, T. W., 2020. Mapping canopy chlorophyll content in a temperate forest using airborne hyperspectral data. *Remote Sens.* 12, 3573. <https://doi.org/10.3390/rs12213573>.
- Hornero, A., North, P., Zarco-Tejada, P., Rascher, U., Martín, M., Migliavacca, M., Hernandez-Clemente, R., 2021. Assessing the contribution of understory sun-induced chlorophyll fluorescence through 3-D radiative transfer modelling and field data. *Remote Sens. Environ.* 253, 112195 <https://doi.org/10.1016/j.rse.2020.112195>.
- Huete, A., Didan, K., Miura, T., Rodriguez, E.P., Gao, X., Ferreira, L.G., 2002. Overview of the radiometric and biophysical performance of the MODIS vegetation indices. *Remote Sens. Environ.* 83 (1–2), 195–213. [https://doi.org/10.1016/S0034-4257\(02\)00096-2](https://doi.org/10.1016/S0034-4257(02)00096-2).
- Jenoh, E.M., Robert, E.M.R., Lehmann, I., Kioko, E., Bosire, J.O., Ngisiange, N., Dahdouh-Guebas, F., Koedam, N., Ling, E., 2016. Wide ranging insect infestation of the pioneer mangrove Sonneratia alba by two insect species along the Kenyan coast. *e0154849* *PLoS One* 11 (5). <https://doi.org/10.1371/journal.pone.0154849>.
- Jia, M., Wang, Z., Wang, C., Mao, D., Zhang, Y., 2019. A new vegetation index to detect periodically submerged mangrove forest using single-tide sentinel-2 imagery. *Remote Sens.* 11 (17), 2043. <https://doi.org/10.3390/rs11172043>.
- Jiang, X., Zhen, J., Miao, J., Zhao, D., Wang, J., Jia, S., 2021. Assessing mangrove leaf traits under different pest and disease severity with hyperspectral imaging spectroscopy. *Ecol. Indic.* 129, 107901 <https://doi.org/10.1016/j.ecolind.2021.107901>.
- Jin, H., Eklundh, L., 2014. A physically based vegetation index for improved monitoring of plant phenology. *Remote Sens. Environ.* 152, 512–525. <https://doi.org/10.1016/j.rse.2014.07.010>.
- Kanning, M., Kühlung, I., Trautz, D., Jarmer, T., 2018. High-resolution UAV-based hyperspectral imagery for LAI and chlorophyll estimations from wheat for yield prediction. *Remote Sens.* 10 (12), 2000. <https://doi.org/10.3390/rs10122000>.
- Kennedy, B.E., King, D.J., Duffe, J., 2021. Retrieval of Arctic Vegetation Biophysical and Biochemical Properties from CHRIS/PROBA Multi-Angle Imagery Using Empirical and Physical Modelling. *Remote Sens.* 13 (9), 1830. <https://doi.org/10.3390/rs13091830>.
- Khanmohammadi, M., Garmarudi, A.B., de la Guardia, M., 2013. Feature selection strategies for quality screening of diesel samples by infrared spectrometry and linear discriminant analysis. *Talanta* 104, 128–134. <https://doi.org/10.1016/j.talanta.2012.11.032>.
- León, A.P., Vina, S.Z., Frezza, D., Chaves, A., Chiesa, A., 2007. Estimation of chlorophyll contents by correlations between SPAD-502 meter and chroma meter in butterhead lettuce. *Commun. Soil Sci. Plan.* 38 (19–20), 2877–2885. <https://doi.org/10.1080/00103620701663115>.
- Li, D., Cheng, T., Zhou, K., Zheng, H., Yao, X., Tian, Y., Zhu, Y., Cao, W., 2017. WREP: a wavelet-based technique for extracting the red edge position from reflectance spectra for estimating leaf and canopy chlorophyll contents of cereal crops. *ISPRS J. Photogram. Remote Sens.* 129, 103–117. <https://doi.org/10.1016/j.isprsjprs.2017.04.024>.
- Li, W., Sun, Z., Lu, S., Omasa, K., 2019. Estimation of the leaf chlorophyll content using multiangular spectral reflectance factor. *Plant, cell & environment* 42 (11), 3152–3165.
- Li, Y., Ma, Q., Chen, J.M., Croft, H., Luo, X., Zheng, T., Rogers, C., Liu, J., 2021. Fine-scale leaf chlorophyll distribution across a deciduous forest through two-step model inversion from Sentinel-2 data. *Remote Sens. Environ.* 264, 112618 <https://doi.org/10.1016/j.rse.2021.112618>.
- Liang, L., Di, L., Huang, T., Wang, J., Lin, L., Wang, L., Yang, M., 2018. Estimation of leaf nitrogen content in wheat using new hyperspectral indices and a random forest regression algorithm. *Remote Sens.* 10 (12), 1940. <https://doi.org/10.3390/rs10121940>.
- Liang, L., Qin, Z., Zhao, S., Di, L., Zhang, C., Deng, M., Lin, H., Zhang, L., Wang, L., Liu, Z., 2016. Estimating crop chlorophyll content with hyperspectral vegetation indices and the hybrid inversion method. *Int. J. Remote Sens.* 37, 2923–2949. <https://doi.org/10.3390/rs10121940>.
- Locherer, M., Hank, T., Danner, M., Mauser, W., 2015. Retrieval of seasonal leaf area index from simulated EnMAP data through optimized LUT-based inversion of the PROSAIL model. *Remote Sens.* 7 (8), 10321–10346. <https://doi.org/10.3390/rs70810321>.
- Loozen, Y., Karssenberg, D., de Jong, S.M., Wang, S., van Dijk, J., Wassen, M.J., Rebel, K. T., 2019. Exploring the use of vegetation indices to sense canopy nitrogen to phosphorous ratio in grasses. *Int. J. Appl. Earth. Obs.* 75, 1–14. <https://doi.org/10.1016/j.jag.2018.08.012>.
- Lu, B., He, Y., Dao, P.D., 2019a. Comparing the performance of multispectral and hyperspectral images for estimating vegetation properties. *IEEE J.-Stars* 12 (6), 1784–1797. <https://doi.org/10.1109/JSTARS.2019.2910558>.
- Lu, S., Lu, X., Zhao, W., Liu, Y., Wang, Z., Omasa, K., 2015. Comparing vegetation indices for remote chlorophyll measurement of white poplar and Chinese elm leaves with different adaxial and abaxial surfaces. *J. Exp. Bot.* 66 (18), 5625–5637. <https://doi.org/10.1093/jxb/erv270>.
- Lu, S., Lu, F., You, W., Wang, Z., Liu, Y., Omasa, K., 2018. A robust vegetation index for remotely assessing chlorophyll content of dorsiventral leaves across several species in different seasons. *Plant Methods* 14 (1), 1–15. <https://doi.org/10.1186/s13007-018-0281-z>.
- Lu, W., Xiao, J., Cui, X., Xu, F., Lin, G., Lin, G., 2019b. Insect outbreaks have transient effects on carbon fluxes and vegetative growth but longer-term impacts on reproductive growth in a mangrove forest. *Agr. Forest Meteorol.* 279, 107747. <https://doi.org/10.1016/j.agrformet.2019.107747>.
- Luo, Y.Y., Vorsatz, L.D., Not, C., Cannici, S., 2022. Landward zones of mangroves are sinks for both land and water borne anthropogenic debris. *Sci. Total. Environ.* 818, 151809 <https://doi.org/10.1016/j.scitotenv.2021.151809>.
- Ma, R.-F., Cheng, H., Inyang, A., Wang, M., Wang, Y.-S., 2020. Distribution and risk of mercury in the sediments of mangroves along South China Coast. *Ecotoxicology* 29 (6), 641–649. <https://doi.org/10.1007/s10646-020-02238-9>.
- Maimaitijiang, M., Sagan, V., Sidike, P., Maimaitiyiming, M., Hartling, S., Peterson, K.T., Maw, M.J., Shakoor, N., Mockler, T., Fritsch, F.B., 2019. Vegetation index weighted canopy volume model (CVMVI) for soybean biomass estimation from unmanned aerial system-based RGB imagery. *ISPRS J. Photogram. Remote Sens.* 151, 27–41. <https://doi.org/10.1016/j.isprsjprs.2019.03.003>.
- Morley, P.J., Jump, A.S., West, M.D., Donoghue, D.N., 2020. Spectral response of chlorophyll content during leaf senescence in European beech trees. *Environ. Res. Commun.* 2 (7), 071002 <https://doi.org/10.1590/10.1088/2515-7620/aba7a0>.
- Neres, J., Dodonov, P., Mielke, M.S., Strenzel, G.M.R., 2020. Relationships between portable chlorophyll meter estimates for the red mangrove tree (*Rhizophora mangle* L.). *Ocean. Coast. Res.* 68 <https://doi.org/10.1590/s2675-28242020068308>.
- Oscos, L.P., Ramos, A.P.M., Moriya, É.A.S., Bavaresco, L.G., Lima, B.C.d., Estrabis, N., Pereira, D.R., Creste, J.E., Júnior, J.M., Gonçalves, W.N., Imai, N.N., Li, J., Liesenberg, V., Araújo, F.F.d., 2019. Modeling hyperspectral response of water-stress induced lettuce plants using artificial neural networks. *Remote Sens.* 11 (23), 2797. <https://doi.org/10.3390/rs11232797>.
- Poças, I., Tosin, R., Gonçalves, I., Cunha, M., 2020. Toward a generalized predictive model of grapevine water status in Douro region from hyperspectral data. *Agr. Forest Meteorol.* 280, 107793 <https://doi.org/10.1016/j.agrformet.2019.107793>.
- Qiao, K., Zhu, W., Xie, Z., 2020. Application conditions and impact factors for various vegetation indices in constructing the LAI seasonal trajectory over different vegetation types. *Ecol. Indic.* 112, 106153 <https://doi.org/10.1016/j.ecolind.2020.106153>.
- Rast, M., Painter, T.H., 2019. Earth observation imaging spectroscopy for terrestrial systems: An overview of its history, techniques, and applications of its missions. *Surv. Geophys.* 40 (3), 303–331. <https://doi.org/10.1007/s10712-019-09517-z>.
- Reyes, J.F., Correa, C., Zuniga, J., 2017. Reliability of different color spaces to estimate nitrogen SPAD values in maize. *Comput. Electron. Agr.* 143, 14–22. <https://doi.org/10.1016/j.compag.2017.09.032>.
- Sadeghi-Tehrani, P., Virlet, N., Hawkesford, M.J., 2021. A Neural Network Method for Classification of Sunlit and Shaded Components of Wheat Canopies in the Field Using High-Resolution Hyperspectral Imagery. *Remote Sens.* 13 (5), 898. <https://doi.org/10.3390/rs13050898>.
- Sathish, C., Nakhawa, A., Bharti, V.S., Jaiswar, A., Deshmukhe, G., 2021. Estimation of extent of the mangrove defoliation caused by insect *Hyblaea puera* (Cramer, 1777) around Dharmtar creek, India using Sentinel 2 images. *Reg. Stud. Mar. Sci.* 48, 102054 <https://doi.org/10.1016/j.rsma.2021.102054>.
- Schwieder, M., Leitão, P.J., Suess, S., Senf, C., Hostert, P., 2014. Estimating fractional shrub cover using simulated EnMAP data: A comparison of three machine learning regression techniques. *Remote Sens.* 6 (4), 3427–3445. <https://doi.org/10.3390/rs6043427>.
- Shah, S.H., Angel, Y., Houborg, R., Ali, S., McCabe, M.F., 2019. A random forest machine learning approach for the retrieval of leaf chlorophyll content in wheat. *Remote Sens.* 11 (8), 920. <https://doi.org/10.3390/rs11080920>.
- Shu, M., Zuo, J., Shen, M., Yin, P., Wang, M., Yang, X., Tang, J., Li, B., Ma, Y., 2021. Improving the estimation accuracy of SPAD values for maize leaves by removing UAV hyperspectral image backgrounds. *Int. J. Remote sens.* 42 (15), 5864–5883. <https://doi.org/10.1080/01431161.2021.1931539>.
- Si, Y., Schlerf, M., Zurita-Milla, R., Skidmore, A., Wang, T., 2012. Mapping spatio-temporal variation of grassland quantity and quality using MERIS data and the PROSAIL model. *Remote sens. Environ.* 121, 415–425. <https://doi.org/10.1016/j.rse.2012.02.011>.
- Singh, D., Singh, S., 2018. Geospatial Modeling of Canopy Chlorophyll Content Using High Spectral Resolution Satellite Data in Himalayan Forests. *Climate Change and Environmental Sustainability* 6 (1), 20–34.
- Slamet, N.S., Dargusch, P., Aziz, A.A., Wadley, D., 2020. Mangrove vulnerability and potential carbon stock loss from land reclamation in Jakarta Bay, Indonesia. *Ocean Coast. Manage.* 195, 105283 <https://doi.org/10.1016/j.ocecoaman.2020.105283>.
- Song, J., Huang, H., Hao, Y., Song, S., Zhang, Y., Su, W., & Liu, H., 2020. Nutritional quality, mineral and antioxidant content in lettuce affected by interaction of light

- intensity and nutrient solution concentration. *Sci. Rep.*, 10(1), 1–9. s41598-020-59574-3.
- Sonobe, R., Yamashita, H., Mihara, H., Morita, A., Ikka, T., 2021. Hyperspectral reflectance sensing for quantifying leaf chlorophyll content in wasabi leaves using spectral pre-processing techniques and machine learning algorithms. *Int. J. Remote Sens.* 42 (4), 1311–1329. <https://doi.org/10.1080/01431161.2020.1826065>.
- Sun, J., Shi, S., Yang, J., Du, L., Gong, W., Chen, B., Song, S., 2018. Analyzing the performance of PROSPECT model inversion based on different spectral information for leaf biochemical properties retrieval. *ISPRS J. Photogram. Remote Sens.* 135, 74–83. <https://doi.org/10.1016/j.isprsjprs.2017.11.010>.
- Sun, J., Yang, J., Shi, S., Chen, B., Du, L., Gong, W., Song, S., 2017. Estimating rice leaf nitrogen concentration: influence of regression algorithms based on passive and active leaf reflectance. *Remote Sens.* 9 (9), 951. <https://doi.org/10.3390/rs9090951>.
- Tagliabue, G., Boschetti, M., Bramati, G., Candiani, G., Colombo, R., Nutini, F., Pompilio, L., Rivera-Caicedo, J.P., Rossi, M., Rossini, M., Verrelst, J., Panigada, C., 2022. Hybrid retrieval of crop traits from multi-temporal PRISMA hyperspectral imagery. *ISPRS J. Photogram. Remote Sens.* 187, 362–377. <https://doi.org/10.1016/j.isprsjprs.2022.03.014>.
- Tian, J., Zhu, X., Chen, J., Wang, C., Shen, M., Yang, W., Tan, X., Xu, S., Li, Z., 2021. Improving the accuracy of spring phenology detection by optimally smoothing satellite vegetation index time series based on local cloud frequency. *ISPRS J. Photogram. Remote Sens.* 180, 29–44. <https://doi.org/10.1016/j.isprsjprs.2021.08.003>.
- Wang, J., Shi, T., Liu, H., Wu, G., 2016. Successive projections algorithm-based three-band vegetation index for foliar phosphorus estimation. *Ecol. Indic.* 67, 12–20. <https://doi.org/10.1016/j.ecolind.2016.02.033>.
- Wang, J., Xu, Y., Wu, G., 2020. The integration of species information and soil properties for hyperspectral estimation of leaf biochemical parameters in mangrove forest. *Ecol. Indic.* 115, 106467 <https://doi.org/10.1016/j.ecolind.2020.106467>.
- Yang, H., Li, F., Hu, Y., Yu, K., 2021. Hyperspectral indices optimization algorithms for estimating canopy nitrogen concentration in potato (*Solanum tuberosum* L.). *Int. J. Appl. Earth. Obs* 102, 102416. <https://doi.org/10.1016/j.jag.2021.102416>.
- Yu, R., Ren, L., Luo, Y., 2021. Early detection of pine wilt disease in *Pinus tabuliformis* in North China using a field portable spectrometer and UAV-based hyperspectral imagery. *For. Ecosyst.* 8 (1), 1–19. <https://doi.org/10.1186/s40663-021-00328-6>.
- Yue, J., Guo, W., Yang, G., Zhou, C., Feng, H., Qiao, H., 2021. Method for accurate multi-growth-stage estimation of fractional vegetation cover using unmanned aerial vehicle remote sensing. *Plant Methods* 17 (1), 1–16. <https://doi.org/10.1186/s13007-021-00752-3>.
- Zhang, C., Ren, H., Liang, Y., Liu, S., Qin, Q., Ersoy, O.K., 2017. Advancing the PROSPECT-5 model to simulate the spectral reflectance of copper-stressed leaves. *Remote Sens.* 9 (11), 1191. <https://doi.org/10.3390/rs9111191>.
- Zhao, Y., Yan, C., Lu, S., Wang, P., Qiu, G.Y., Li, R., 2019. Estimation of chlorophyll content in intertidal mangrove leaves with different thicknesses using hyperspectral data. *Ecol. Indic.* 106, 105511 <https://doi.org/10.1016/j.ecolind.2019.105511>.
- Zhen, J., Jiang, X., Xu, Y., Miao, J., Zhao, D., Wang, J., Wang, J., Wu, G., 2021. Mapping leaf chlorophyll content of mangrove forests with Sentinel-2 images of four periods. *Int. J. Appl. Earth. Obs* 102, 102387. <https://doi.org/10.1016/j.jag.2021.102387>.
- Zovko, M., Žibrat, U., Knapić, M., Kovacić, M.B., Romić, D., 2019. Hyperspectral remote sensing of grapevine drought stress. *Precis. Agric.* 20 (2), 335–347. <https://doi.org/10.1007/s11119-019-09640-2>.
- Zulfa, A., Norizah, K., Hamdan, O., Zulkifly, S., Faridah-Hanum, I., Rhyma, P., 2020. Discriminating trees species from the relationship between spectral reflectance and chlorophyll contents of mangrove forest in Malaysia. *Ecol. Indic.* 111, 106024 <https://doi.org/10.1016/j.ecolind.2019.106024>.